A deep ocean acoustic noise floor, 1–800 Hz

J. Berger, J.-R. Bidlot, M. A. Dzieciuch, W. E. Farrell, P. F. Worcester, and R. A. Stephen

---

A deep ocean acoustic noise floor, 1–800 Hz

J. Berger,[1,a)] J.-R. Bidlot,[2] M. A. Dzieciuch,[1] W. E. Farrell,[3] P. F. Worcester,[1] and R. A. Stephen[4]

[1]*University of California San Diego SIO-IGPP, 9500 Gilman Drive, Mail Code 0225, La Jolla, California 92093-0225, USA*
[2]*European Centre for Medium-Range Weather Forecasts, Reading, England*
[3]*Del Mar, California 92014, USA*
[4]*Woods Hole Oceanographic Institution, Woods Hole, Massachusetts 02543, USA*

The ocean acoustic noise floor (observed when the overhead wind is low, ships are distant, and marine life silent) has been measured on an array extending up 987 m from 5048 m depth in the eastern North Pacific, in what is one of only a few recent measurements of the vertical noise distribution near the seafloor in the deep ocean. The floor is roughly independent of depth for 1–6 Hz, and the slope ($\sim f^{-7}$) is consistent with Longuet-Higgins radiation from oppositely-directed surface waves. Above 6 Hz, the acoustic floor increases with frequency due to distant shipping before falling as $\sim f^{-2}$ from 40 to 800 Hz. The noise floor just above the seafloor is only about 5 dB greater than during the 1975 CHURCH OPAL experiment (50–200 Hz), even though these measurements are not subject to the same bathymetric blockage. The floor increases up the array by roughly 15 dB for 40–500 Hz. Immediately above the seafloor, the acoustic energy is concentrated in a narrow, horizontal beam that narrows as f^{-1} and has a beam width at 75 Hz that is less than the array resolution. The power in the beam falls more steeply with frequency than the omnidirectional spectrum.
© 2018 Acoustical Society of America. https://doi.org/10.1121/1.5025042

I. INTRODUCTION

Events on the marine-atmosphere boundary layer radiate sound into the ocean. Above about 6 Hz, ships are an important source of this sound, and their influence must be discounted in order to study the acoustic signal in this band radiated by windsea processes (Farrell *et al.*, 2016). For positions in the deep ocean well below the surface conjugate depth and for frequencies between 50 and 1000 Hz, the two phenomena can be qualitatively distinguished by their characteristic omnidirectional spectra. The cumulative effect of radiation from distant ships falls steeply with frequency and increases with elevation above the bottom. Wind-correlated noise, on the other hand, has a relatively flat spectrum and varies little with elevation (Morris, 1976, 1978; Gaul *et al.*, 2007; Duennebier *et al.*, 2012). Here we analyze data from a vertical hydrophone array fortuitously positioned for three days beneath the center of an anticyclone from which there was virtually no windsea acoustic radiation.

The acoustic floor is not unique, but varies with geographic location, observation depth, and time. This report details the acoustic floor during June–July 2013 at station OBSANP [Ocean Bottom Seismometer Augmentation in the North Pacific, 33° 25.135′ N, 137° 40.948′ W, Stephen *et al.* (2014)]. A Distributed Vertical Line Array (DVLA) receiver extending up 987 m from the seafloor was deployed at the location that a deep vertical line array receiver had previously been deployed during the 2004–2005 SPICEX experiment, for which Farrokhrooz *et al.* (2017) reports on the ambient noise measurements. The deepest hydrophone during SPICEX was at 4218 m depth, which is slightly deeper than the depth of the shallowest hydrophone during OBSANP (4061 m). The OBSANP ambient noise measurements can be viewed as extending the measurements made during SPICEX down to 12 m above the seafloor, albeit nearly a decade later. The goal is to understand better the spatial and directional variation of the acoustic floor at one place and time in the deep ocean when the wind overhead is negligible and ship interference least. Other previous measurements of the vertical noise distribution near the seafloor to which the results reported here can be compared include those made during the U.S. Navy's 1973 CHURCH ANCHOR (Morris, 1978) and 1975 CHURCH OPAL (Gaul *et al.*, 2007) experiments. Farrokhrooz *et al.* (2017) provide a summary of the relevant results, referring to measurements at site B of CHURCH ANCHOR as FLIP73. In addition, Anderson (1979) reports on vertical directional spectra measured during CHURCH ANCHOR.

Measurement and modeling of sound radiated from the ocean surface has been in decline since its acme decades ago (Kerman, 1988, 1993; Buckingham and Potter, 1995). Since then, there has been great progress both in modeling ocean weather through the assimilation of remote sensing data, and also in modeling the wave field (Janssen, 2008). Such models support the calculation of low frequency ($f \lesssim 1$ Hz) acoustic and seismic radiation due to oppositely directed wave components, as first enunciated by Longuet-Higgins (1950) and Hasselmann (1963), and applied in many later studies, e.g., Orcutt *et al.* (1993), Kedar *et al.* (2008), Ardhuin *et al.* (2011, 2013), and Peureux and Ardhuin (2016). In addition,

fixed and airborne instrumentation allows direct measurement of the directional wave spectrum over meter to kilometer-sized ocean patches (Yurovskaya *et al.*, 2013; Leckler *et al.*, 2015; Lenain and Melville, 2017) and a similar frequency range.

At higher frequencies, the situation is not so good. There is a plethora of models for the acoustic source physics, but it is not currently possible to calculate the acoustic radiation from ocean observables. [Wilson (1980) derived an empirical relationship between sound and the whitecap index for $f > 200$ Hz, but the index was effectively a surrogate for U_{10}.] Rather, as has been the practice for decades, the acoustic spectrum, $F_p(f, U)$, is related to overhead wind, U, from which it is trivial to deduce the strength of a dipole layer, $D(f, U) = F_p(f, U)/\pi$ (Wilson, 1983). This simplistic association ignores not only the radiation pattern but also the spatial variability of the acoustic sources induced by the wind field.

Following a recommendation made decades ago (Buckingham and Potter, 1995, p. 482), SI units are used throughout. To obtain traditional units (dB re μPa^2/Hz), multiply the values by 10^{12}, and take ten times the base 10 logarithm. Thus, 1×10^{-6} Pa^2/Hz maps to 60 dB re μPa^2/Hz.

II. OBSANP INSTRUMENTATION

The OBSANP vertical line array (VLA) comprised 27 nodes spanning 975 m. Each node was an autonomous hydrophone module (HM) with integral data recorder (digitization rate 1953.125 Hz). Pressure data from two ocean bottom seismometer (OBS) systems, LPB and LPD (long period seismometer systems B and D), deployed near the VLA, are briefly mentioned: the transducers are described in Farrell *et al.* (2016). Their spectra augment the band 3–20 Hz where the HMs are limited by self-noise. These data were recorded at 1000 Hz. Their response was calibrated against the differential pressure gauge (DPG) on LPB.

Technical specifications of the HMs are given in Worcester *et al.* (2009, 2013). All systems were individually calibrated. The HM self-noise was measured in the laboratory using a dummy hydrophone in which the ceramic was replaced by a capacitor. It is closely fit by the model $F_{HM} = 4 \times 10^{-5} f^{-2}$, between 1 and 100 Hz, after correcting the laboratory measurements to account for the 2 dB loss in hydrophone sensitivity at the pressure near the deep seafloor (Fig. 3). At 100 Hz, the measured self-noise is more than 10 dB lower than the observed acoustic floor.

A complete description of the exercise is provided in Stephen *et al.* (2014). The ocean depth at the site is 5048 m, and the deepest node, HM148, was 12 m off the bottom. The measured sound speed profile gave a conjugate depth of 3670 m.

Observations of wind and wave conditions above the experiment site are inadequate. Although extensive meteorological data were recorded on R/V Melville, during the three-day interval studied here she was, on average, 50 km to the north of the VLA location. However, as shown previously, the wind speed recorded on R/V Melville during OBSANP is closely matched by the ECMWF wind model, interpolated onto the R/V Melville track (Farrell *et al.*, 2016, Fig. 4). Thus, we use the ECMWF model for the VLA location as an acceptable proxy for the actual conditions.

III. EPOCH SELECTION AND ANALYSIS

Slightly over two weeks of VLA data were recorded. A small number of non-contiguous 10-min epochs with exceptionally low power over the whole band were identified (Fig. 1). Several related approaches gave a similar selection.

As the figure shows, the chosen epochs fell at times when the wind above was tiny. A synoptic view of the meteorology during the data interval is shown in Fig. 2. A strong anticyclone was positioned over the location of the OBSANP VLA. At the beginning, the center of the weather pattern was about 300 km West, and over the interval, the center drifted south about 200 km as a band of extremely high winds pushed down from the North. This weather situation was quite different from the cold front ten days later studied previously (Farrell *et al.*, 2016).

For wave number analysis, the VLA was partitioned into four sub-arrays, each with uniform 10 m node spacing (Table I). Three 60 m sub-arrays were centered 42, 132, and 957 m off the bottom (Top, Middle, Bottom). A sub-array Lower, with 150 m aperture, was formed by linking the Middle and Bottom 60 m sub-arrays with two intermediate nodes. The short sub-arrays sampled vertical variation in the wave field. The long array yields maximum directional resolution.

IV. SPECTRA AND CROSS-SPECTRA

It is appropriate to split the analysis into two overlapping frequency bands, a low frequency band, $1 < f < 50$ Hz, and a high frequency band, $10 < f < 1000$ Hz. This facilitates mixing linear and logarithmic frequency scales in the figures without sacrificing resolution. It also recognizes the difference in the physical sources exciting the acoustic floor: wind sea transitioning to ships across the lower band but ships alone in the upper band.
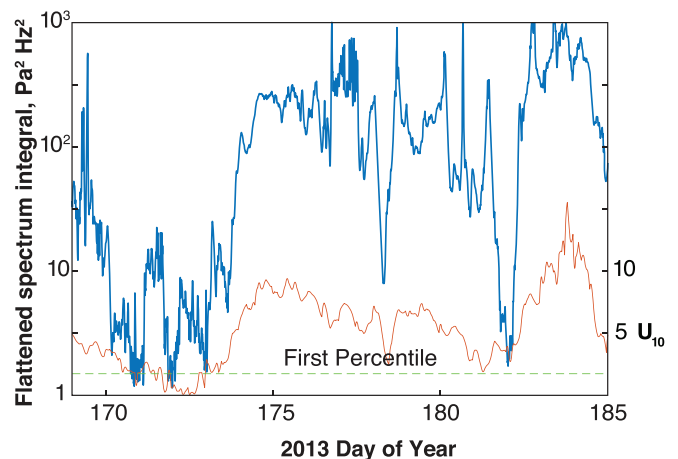
FIG. 1. The 16.9 days of data were split into 2441 ten-minute epochs. Spectra of all epochs for the deepest node (148) were divided by 0.0014 f^{-2} (which generally flattened them) and integrated from 5 to 800 Hz. We selected the epochs for which the integral of the flattened spectrum at this node was below the first percentile: there were 19 totaling 3.17 data-hours. (blue) The integral of the flattened spectral estimates of the pressure. (red) The ECMWF hourly wind speed at the VLA location (m/s). (green) The first percentile level of the flattened pressure spectrum.

FIG. 2. The ECMWF wind field indicates a strong anticyclone with high pressure (contours) centered about OBSANP (red squar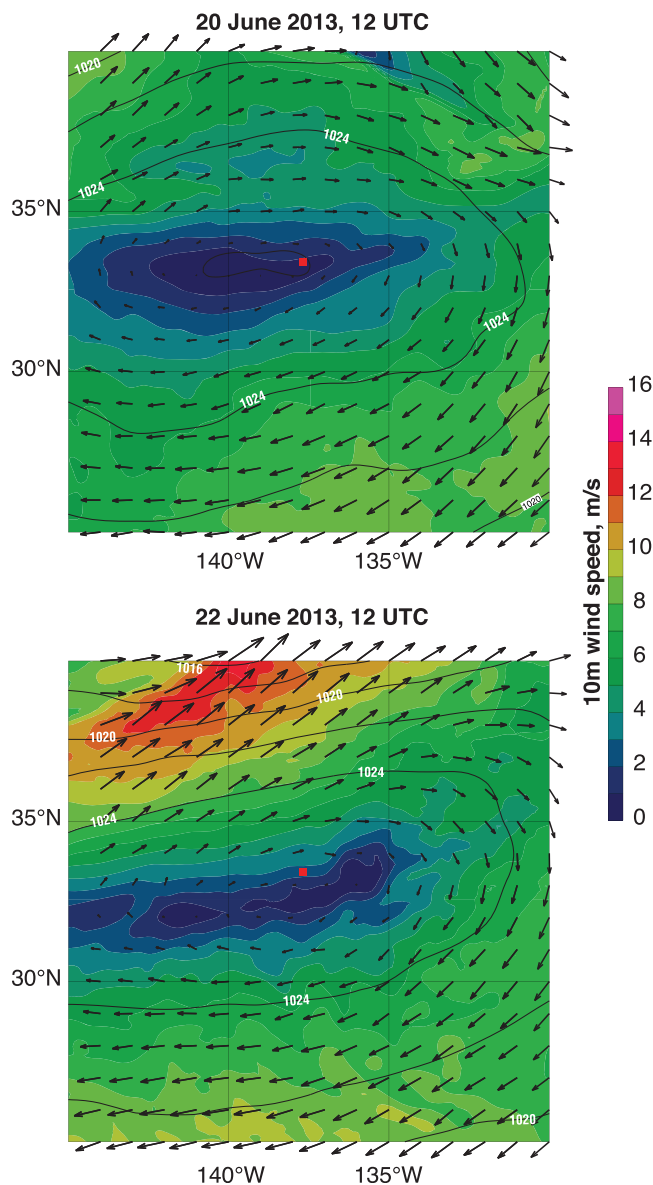e) for two days spanning the acoustic floor epochs. This model is from the ECMWF operational analysis product for those days. (Top) 20 June 2013, 12 UTC, ordinal date 171.5. (Bottom) 22 June 2013, 12 UTC, ordinal date 173.5.

A. Low frequencies ($1 < f < 50$ Hz)

The acoustic floor in the band $1 < f < 50$ Hz experiences a transition near a spectral minimum at $f \approx 6$ Hz. For frequencies below 6 Hz, the acoustic floor falls approximately

TABLE I. Parameters of the four VLA sub-arrays. Elements are all spaced 10 m apart.

Array	Aperture (m)	Number of Elements	Acoustic center (m)	
			Depth	Elevation
Top	60	7	4091	957
Middle	60	7	4916	132
Bottom	60	7	5006	42
Lower	150	16	4951	87

as f^{-7} and is driven by Longuet-Higgins radiation from non-linear interactions of oppositely-directed surface waves. For higher frequencies, the acoustic floor rises like f^2, which is the same slope as observed in cavitation noise from ships (Audoly *et al.*, 2014, Fig. 9).

1. Spectra

Up the 975-meter array aperture and in the L–H band, the increase in acoustic floor is 10 dB or less (Fig. 3, 2 Hz). For frequencies in the ship noise region and higher than the HM self-noise limit of 20 Hz, the spectrum rises by more than 20 dB.

The transition at ≈ 6 Hz on the deepest VLA nodes (purple, blue) is obscured in these data because the self-noise of the sensors hides the ocean signal. The self-noise, presumed to arise from f^{-1} electronic noise, has a power spectrum falling like f^{-2}, as indicated.

The f^{-7} low frequency approximation to the spectra (dash black line) evaluates to 0.004 Pa^2/Hz at 1 Hz. This is comparable to the lowest levels at this frequency reported by Farrell and Munk (2013, Fig. 1) and Duennebier *et al.* (2012, Fig. 6).

2. Nearest neighbor cross-spectra

Cross-spectra between nearest neighbors give further insight into the inhomogeneity of the acoustic field. They also provide another marker of the split in physics between the depth-independent f^{-7} shape at the low end of the band and the depth-varying f^2 shape over the upper decade of the band.

The coherence between nearest neighbors for all sensor pairs (10 m separation) varies sharply both with frequency and with height above the bottom (Fig. 4). The dip at 6 Hz is narrow at sub-array Top [Fig. 4(a)], but is artificially broadened for sub-array Lower (b) because of sensor noise. At sub-array Top and $f > 20$ Hz coherence does not vary significantly across the 60 m aperture, indicating a homogeneous acoustic field. At sub-array Lower, the rise in coherence with frequency does not flatten until 30 Hz, and neighbors near the bottom are less coherent than those higher up.

The middling coherence between neighbors for frequencies below 3 Hz (2 Hz for Lower) is not understood. The spectrum is some 20 dB below the level that occurs for wind speeds of 6 m/s and larger, and the drop has been modeled as a consequence of a precipitous fall in the overlap integral (Farrell and Munk, 2013). If the sound is indeed residual radiation from the sea surface above, a higher degree of coherence might be expected.

B. High frequencies ($10 < f < 800$ Hz)

Sound in the deep ocean over the band $10 < f < 800$ Hz) has been studied for decades under a variety of wind and ship noise conditions.

The novelty in our approach is to focus attention on an interval of extraordinarily low winds extending over a large area of the ocean surface. This allows us to assess shipping noise over a broad frequency range. Our results agree in general with earlier work, with minor extensions.
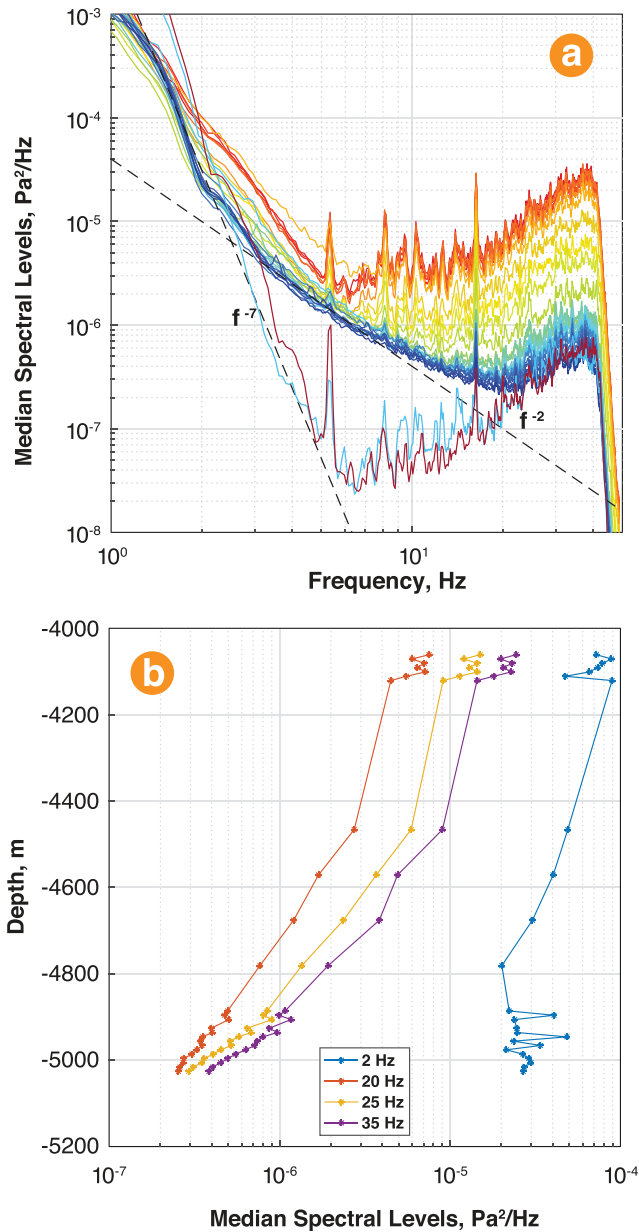
FIG. 3. (a) Median spectral estimates for a Nyquist of 50 Hz and a resolution of 0.1 Hz. The deepest VLA node (5036 m) is shown in dark purple and the shallowest (4061 m) in red. The two lower spectra, which define the minimum near 6 Hz, are of data from low noise hydrophones on two near-by OBSs. There appears to be a calibration discrepancy at the lowest frequencies. The black dash lines are the functions $0.004 \times f^{-7}$ and $4 \times 10^{-5} f^{-2}$. (b) The variation in power (averaged over 0.5 Hz) with depth for the indicated frequencies.

1. Spectra

In this band, the power at the top of the array is 16 dB higher than at the bottom for $f = 40$ Hz (Fig. 5). The same vertical gradient holds up to 500 Hz, above which the spectra for the nodes at Top and Middle become lower, narrowing the range. The cause of the quieting is not understood.

Median spectra of the seven individual elements of sub-arrays Top and Bottom are plotted against linear frequency in Fig. 6. This emphasizes the closeness of the f^{-2} models and the relatively small variation in power over the 60 m apertures.

The spectra for nodes near the bottom (blue) are typical of deep ocean conditions when there are no ships within the
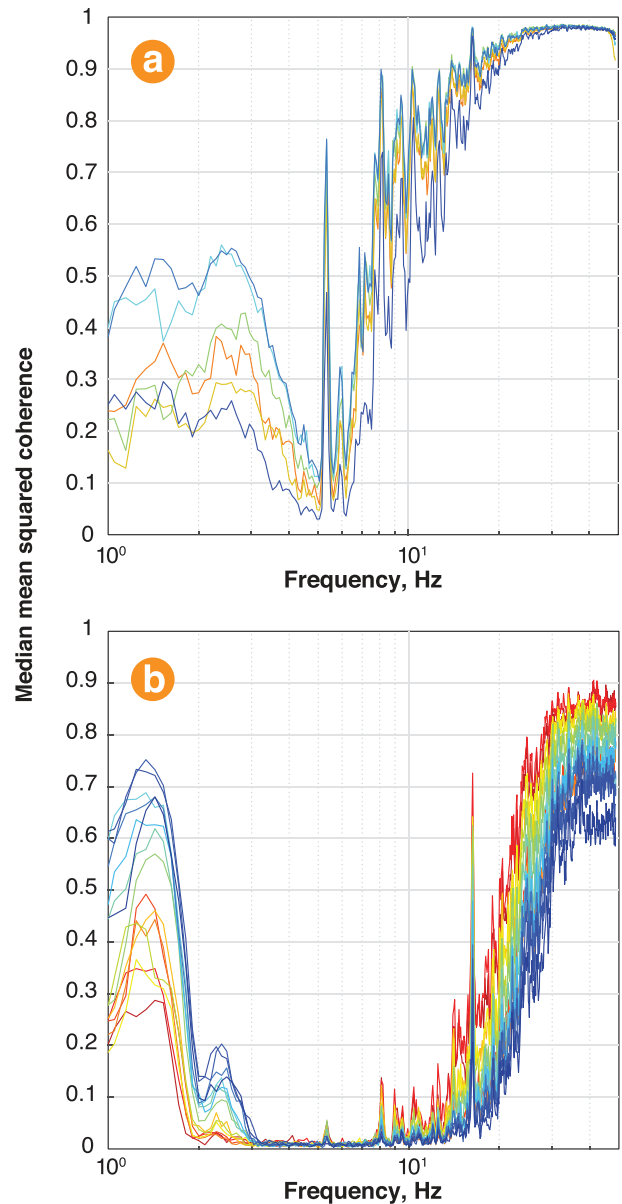

FIG. 4. (a) On sub-array Top, the coherence between neighboring nodes falls precipitously over the octave from 10 to 5 Hz. (b) For the 16 nodes comprising sub-array Lower, the fall occurs between 25 and 15 Hz, and is a consequence of instrumentation self-noise dominating the lower signal levels encountered nearer the bottom.

direct path range and the overhead wind is small. Section VII B discusses these results in relation to earlier observations.

The narrow peak at 360 Hz is a line generated by R/V Melville, which was 45 km north during these epochs. Except for the line, R/V Melville radiation at other frequencies was lower than the acoustic floor. Fortunately, R/V Melville was positioned between convergence zones. The transmission loss to a deep receiver at a range of 40–50 km is estimated to exceed 55 dB (Stephen *et al.*, 2014, Fig. 4.3).

2. Nearest neighbor cross-spectra

The coherence between neighbors shows negligible variation with position for sub-array Top (Fig. 7, upper red cluster), falling to 0.5 at 300 Hz. In contrast, the coherence

FIG. 6. Median spectra for the elements of the sub-arrays Top (red) and Bottom (blue) are tightly clustered and fall like f^{-2} over a wide frequency range. The blue are the seven lowest (blue) spectra of Fig. 5 and the red are the seven highest (red) in the figure.
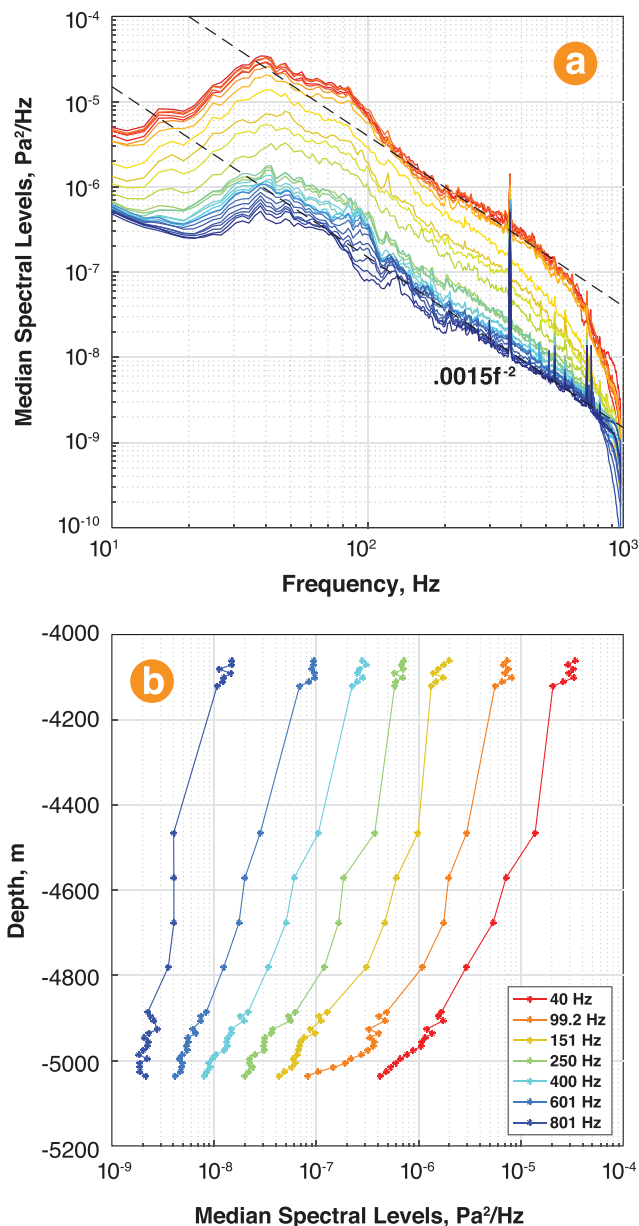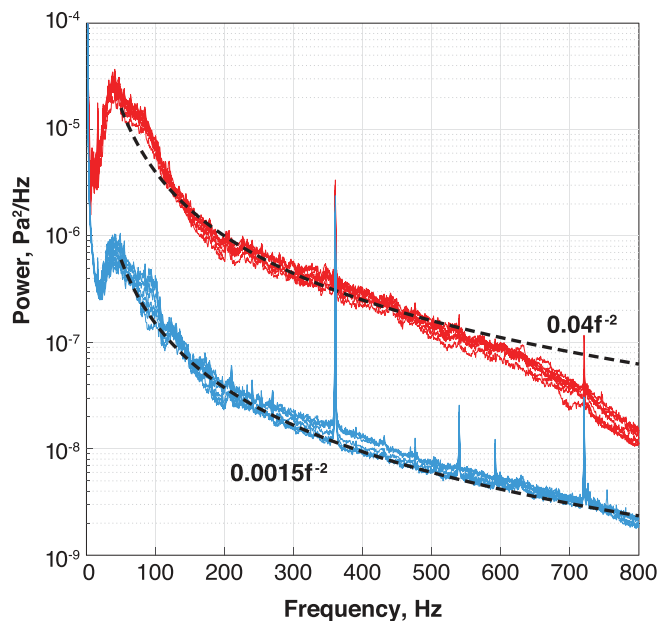

FIG. 5. (a) The spectrum of the acoustic floor rises about 16 dB from the bottom element of the VLA (blue, 5036 m) to the top element (red, 4081 m) for frequencies between 40 and 500 Hz. The lower dash line is the function $0.0015 \times f^{-2}$; the upper dash line is parallel and 16 dB higher. (b) The profile of the power up the array at selected frequencies shows the gradient is least at the highest frequency (blue) where the spectrum is smallest.

across the aperture of sub-array Lower falls to 0.5 by 100 Hz or less (Fig. 7, lower curves). Neighbors near the bottom of Lower (Fig. 7, blue) are less coherent than neighbors near the top, 150 m away (Fig. 7, yellow). It is curious that for frequencies above 300 Hz, the coherence for each sensor pair of sub-array Top (red) is less than for Middle (yellow-green).

V. FREQUENCY-WAVE NUMBER SPECTRA

Conventional f, κ spectra were calculated for the selected epochs of each sub-array and medians taken. The frequency resolution was 0.48 Hz, and Kaiser wave number tapering utilized, giving half-power beam widths (HPBW) 2×0.062 and 2×0.025 radians/m for the shorter and longer sub-arrays,

respectively (van Trees, 2004, Sec. 3.1.1.9). In all cases, the energy has a strong horizontal polarization for $20 \lesssim f \lesssim 400$ Hz. For both apertures, the observed beam width is not significantly broader than the theoretical beam width for the chosen window.

A. Low frequencies

The low frequency f, κ spectra show that the beam shape is similar on the three short sub-arrays with twice the breadth on the longer [Figs. 8(a) and 8(b), and 8(c) vs 8(d)]. The beam is less distinct on the lower sub-arrays [Figs. 8(b), 8(c), and 8(d)] for $f \lesssim 20$ Hz due to sensor noise, which is the cause of the vertical yellow and red banding.

Above 20 Hz, the beam has about the width of the analysis window (green horizontal dash lines). At 50 Hz, this places upper limits on the natural HPBW of 14 (39) degrees for the 150 m (60 m) apertures. Because the natural HPBW is not resolved, the expected increase in HPBW with distance above the bottom is obscured.

The spectrum for the Top sub-array is plotted with a 15 dB upward shift in the color palette, in accordance with the rise in power with distance above the bottom (see Fig. 6). Even with this equalization, the off-beam power is much less on Top than on the other three panels. The stronger main lobe for Top is also apparent in Fig. 10. If the natural beam width were resolvable, the difference would be even more striking.

The spectrum for Top also clearly shows the disappearance of the beam for frequencies $\lesssim 6$ Hz. As has been noted, this is a consequence of the diminished strength of ship radiation relative to windsea energy.

B. High frequencies

The f, κ spectra for high frequencies (Fig. 9) have been multiplied by $(2\pi f)^2$ to give spectrograms with
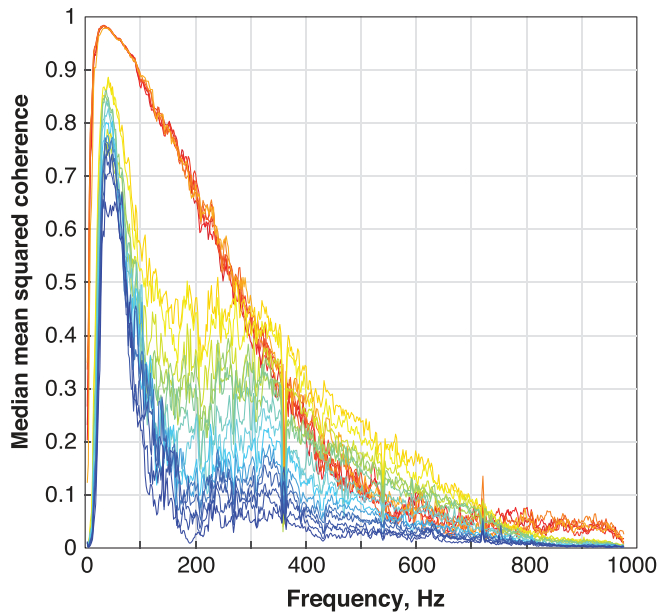
FIG. 7. The coherence between neighboring nodes on sub-array Top (red) is distinctly higher than the coherence between neighboring nodes on sub-array Lower (blue to yellow) for $f < 250$ Hz. For Lower, the coherence between the bottom node pair is a small fraction of that between the upper pair, 150 m further above the sea floor.

balanced dynamic range. In addition, the color palette is shifted 10 dB for Top [Fig. 9(a)] to compensate for the higher spectral levels.

For the three sub-arrays near the bottom [Figs. 9(b), 9(c), and 9(d)], the appearance of the horizontal beam is similar to its expression at low frequencies (Fig. 8), being largely confined to the HPBW of the analysis window. There is, however, a slight broadening between 50 and 100 Hz, where the power spectrum has its maximum. The spectrogram for Top [Fig. 9(a)] shows significant energy well

outside the Kaiser HPBW, with an apparent upward tilt. This seems to be an artifact of the display, for κ_z profiles of the beam at several frequencies show the 3 dB points close to the Kaiser theory (see below, Fig. 10).

The 360 Hz radiation from Melville (see Fig. 6) is striking in that it covers the entire wave number range. One interpretation is that this may be due to irregular phase shifts occurring on a time scale shorter than the 10 min analysis epoch.

VI. ACOUSTIC FLOOR BEAM

As is clear in Figs. 8 and 9, the energy of the acoustic floor in the deep ocean is concentrated in a narrow, horizontally polarized beam, as was reported many years ago (Anderson, 1979). Measurements with horizontal arrays in this part of the Pacific have shown that most of this energy comes from the north (Gaul *et al.*, 2007, Fig. 6). The fact that the beams are not significantly broader than the wave number resolution for either aperture shows that the natural width is no greater than the resolution of the 150 m sub-array (Lower).

A. Beam shape

Profiles of the median beams, $F(\kappa_z, f)$, show consistency in both direction and shape for frequencies between 20 and 400 Hz at all four sub-arrays (Fig. 10). The beam width is least for Lower, the sub-array with largest aperture.

The profiles for Top [Fig. 10(a)] show a slight shift to positive wave numbers at high frequencies, whereas the profiles for Middle and Bottom [Figs. 10(b) and 10(c)] shift towards negative wave numbers. This is evident also in the median f, κ_z spectra (Fig. 9). The f, κ_z spectra for individual windows show deviations in direction of up to ±5 degrees.

There is no evidence of the flat topped "pedestal" shape, characteristic of the acoustic floor at the axis of the sound
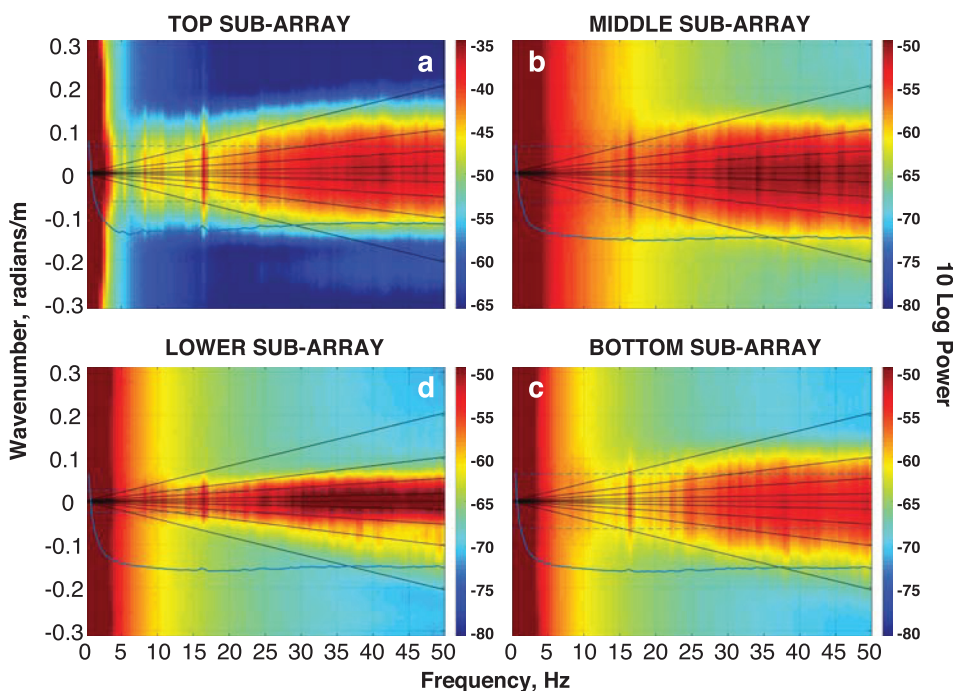
FIG. 8. The low frequency portion of the median f, κ spectra shows a strong beam with horizontal polarization. The beam tapers off at low frequencies, becoming indistinct at about 20 Hz. The straight black lines correspond to phase speeds of ±1530, ±3060, ±5800, and ±17 390 m/s. Assuming a propagation speed of 1530 m/s, these correspond to directions with respect to the horizontal of 90, 30, 15, and 5 degrees. The horizontal dash lines delimit the broadside HPBW for a Kaiser weighting. The HPBW and the data for the 150 m sub-array are both less than half that of the three 60 m sub-arrays. The irregular blue curve shows the spectrum integrated over wave number.

FIG. 9. Median f, κ spectra for the entire frequency range, normalized by $(2\pi f)^2$. For further definitions, see Fig. 8.
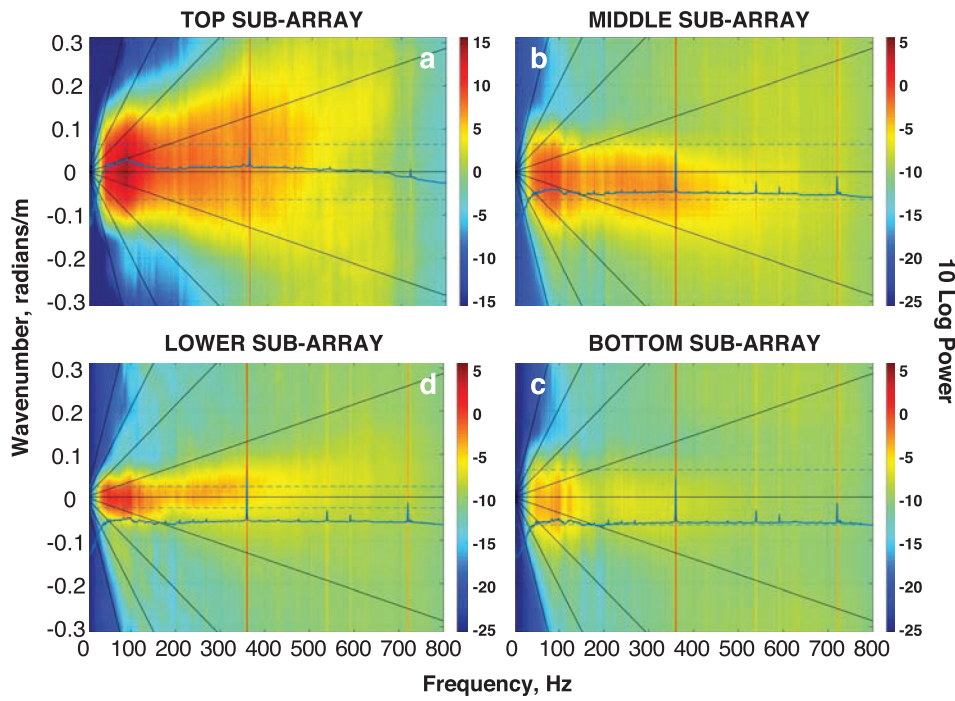
channel (Dashen and Munk, 1984, Fig. 1) and deeper (Sotirin and Hodgkiss, 1990, e.g., Fig. 9; Wagstaff, 2005, Fig. 7).

The ratio of beam power to off-axis power at, say, $\kappa_z = \pm 0.2$ radians/m is greatest at a frequency of 50 Hz (red). At 800 Hz, the spectrum is uniform in wave number with no visible vestige of the beam (violet). Of course, with a spatial Nyquist of 0.05 cycles/m, the energy of short waves with

frequencies above 75 Hz aliases into the ± 0.05 cycles/m band. There are three such foldings by 375 Hz.

The half power beam width for the shorter sub-arrays is consistently in the neighborhood of 0.15 radians/m (Table II). For the longer sub-array, it is about half this value. In both cases, the theoretical broadside beam width with Kaiser weighting is slightly less than the observed HPBW. At 100 Hz, a beamwidth of 0.08 radians/m is equivalent to an angular width of 11°.
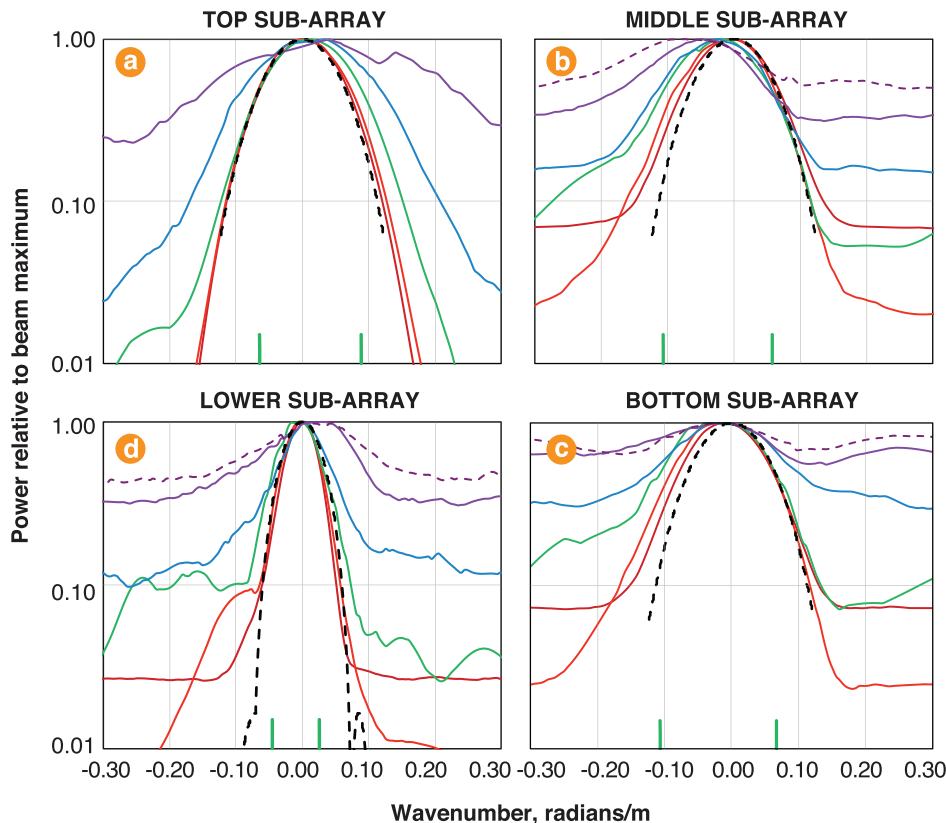
FIG. 10. Beam wave number profiles, when scaled to the maximum at each frequency, show consistent shape and direction. The profile frequencies are 24.8 Hz (red), 49.6 Hz (orange), 99.7 Hz (green), 199.8 Hz (blue), 399.6 Hz (purple), and 499.7 Hz (purple dash). The black dash line is the theoretical profile for Kaiser weighting and a broadside direction. The green ticks inside the x-axis indicate the ± 3 dB points of the 100 Hz beam.

J. Acoust. Soc. Am. **143** (2), February 2018

Berger *et al.*   1229

Array	Frequency, Hz					Average	Kaiser Model
	10	25	50	100	200		
Top	0.138	0.136	0.138	0.153	0.211	$0.15 \pm .07$	0.128
Middle	–	0.142	0.119	0.164	0.168	$0.15 \pm .02$	0.128
Bottom	–	0.140	0.139	0.173	0.223	$0.17 \pm .04$	0.128
Lower	0.080	0.062	0.064	0.077	0.085	$0.062 \pm .03$	0.050

B. Beam power

The profiles of the beams are smooth functions of vertical wave number and frequency. The total power in the beam for array a as a function of frequency can thus be approximated by

$$F_{a,beam}(f) = \int_{-3\,dB(f)}^{3\,dB(f)} F_a(\kappa_z, f)\, d\kappa_z$$
$$\approx HPBW_a(100) F_a(0, f),\quad (1)$$

where $HPBW(100)$ is the beam width at 100 Hz. This neglects the small variation in HPBW with frequency (see Table II), and the small variations in beam direction. We find that the power in the beam falls like f^{-3}, one degree faster than the f^{-2} decrease in the omnidirectional spectrum (Fig. 11).

As a consequence, the power in the beam relative to the flanks decreases the greater the frequency (Fig. 10). This is quantified by the ratio F_{beam}/F_{tot}, where

$$F_{a,tot}(f) = \int_{-\pi/10}^{\pi/10} F_a(\kappa_z, f) d\kappa_z.\quad (2)$$

Assuming a white spectrum at high frequencies, $F_{beam}/F_{tot} \rightarrow HPBW/(\pi/5)$. Using the averages in Table II), this gives

$$\lim_{f \gg 50} \frac{F_{beam}}{F_{tot}} = 0.24,\ 60\ m\ array \quad (3)$$

$$= 0.11,\ 150\ m\ array. \quad (4)$$

The plots of beam power in Fig. 11 are truncated at the frequency where the beam power is within a few dB of this ratio. The limiting frequency is lowest at Top [Fig. 11(a)], where the omnidirectional power is greatest. The limiting frequency is highest at Lower [Fig. 11(d)], which has the largest aperture and quietest environment.

VII. DISCUSSION

A. Low frequency spectra

From 1 Hz to approximately 6 Hz, the acoustic floor is determined by L–H radiation from interacting gravity waves on the ocean surface. The *prima facia* evidence for this is the steep ($\sim f^{-7}$) fall in the spectrum, which is clear in the OBS spectra [Fig. 3(a) blue purple]. We infer were it not for sensor noise, the VLA spectra for the deep nodes (Fig. 3 blue, green) would be sub-parallel to those of the top nodes (red, orange, yellow) filling the triangular void between 3 and 20 Hz. Under stronger winds, the spectrum is some 20 dB above the acoustic floor, but has roughly the same slope [Farrell and Munk (2010, Fig. 4); Duennebier *et al.* (2012, Fig. 6); Farrell and Munk (2013, Fig. 1)].

Based upon a numerical model of L–H radiation, and using OBS data from the Cascadia array, Peureux and Ardhuin (2016) concluded that the energy arises from wave–wave interactions over the ocean surface within
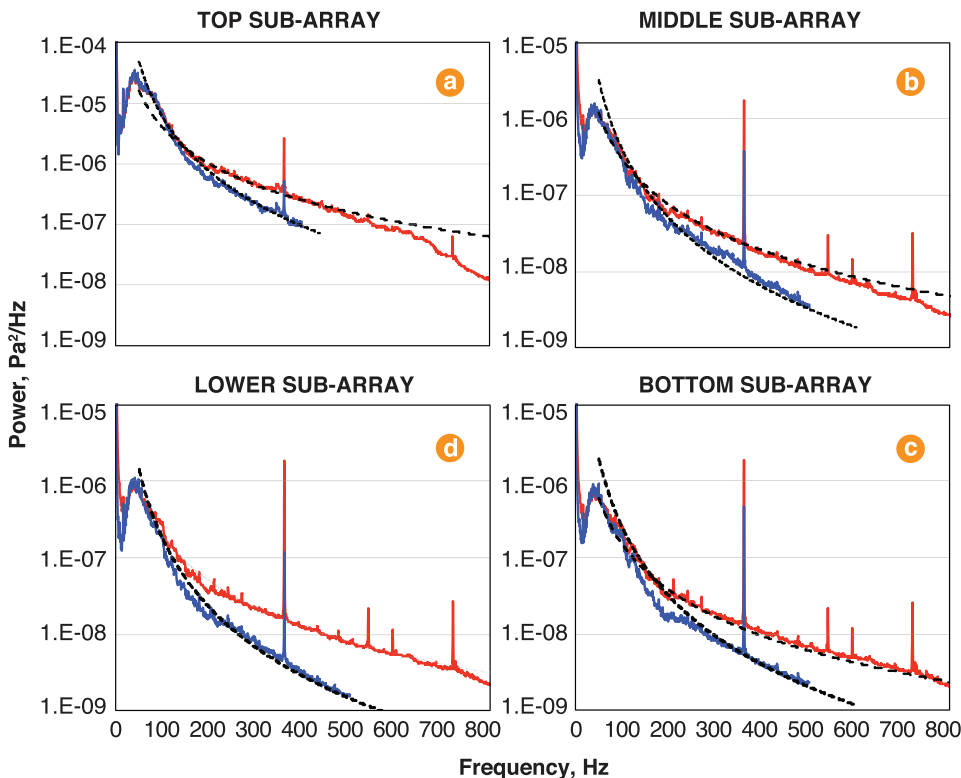
FIG. 11. The power in the beam (blue) decreases with frequency more quickly than the total power (red) for all four sub-arrays. For the omnidirectional spectrum (red), the power decreases like f^{-2} (black dash). The individual spectra comprising these omnidirectional medians for Top and Bottom are shown in Fig. 6. The beam power (blue) is well approximated by the model $\alpha \times f^{-3}$ (lower black dash line) with $\alpha = 6$, 0.4, 0.25, and 0.18 for (a), (b), (c), and (d), respectively.

100 km of the observation point. Furthermore, the correlation length of their numerical wave models was of the same distance or greater, so that the L–H source could be treated as a uniform dipole layer. Their results were most convincing for moderate and strong winds, and they attribute poorer results for low wind speed to deficiencies in the ocean wave model.

The dominance of near-overhead sources is supported by the OBSANP data. The vertical gradient in the VLA observations is small, at least at the lower half of the band, where the acoustic signal is above the sensor noise floor [Fig. 3(b), 2 Hz]. Furthermore, the coherence between OBS pressure and vertical velocity shows unambiguous organ pipe resonances (not shown), similar to those in Guralnik et al. (2013, Fig. 7).

The Peureux and Ardhuin (2016) model consisted of a uniform water layer over an elastic half space. Neglecting the ocean sound speed profile is a weakness in this model because it precludes significant long-range propagation from surface sources to receivers beneath the conjugate depth. The long range propagation of wind noise has been modeled by Evans and Carey (2010), but only at 200 Hz and for receivers in the sound channel.

B. High frequency spectra

Farrokhrooz et al. (2017) compared ambient noise measurements from the 2004–2005 SPICEX experiment with those from the 1973 CHURCH ANCHOR (FLIP73) (Morris, 1978) and 1975 CHURCH OPAL (Gaul et al., 2007) exercises, all of which provided information on the vertical noise distribution in the eastern North Pacific Ocean. The OBSANP measurements can now be compared with those from these earlier experiments. In addition, the OBSANP measurements can be compared with those from a bottom-mounted hydrophone at the Aloha Cabled Observatory (ACO) north of Oahu, HI, in the central North Pacific Ocean, and with those measured at the U.S. Navy test range in the Tongue of the Ocean (TOTO) in the Bahamas, which is sheltered from Atlantic Ocean ship noise. Neither ACO nor TOTO, however, provide information on the vertical noise distribution.

The OBSANP and SPICEX measurements were made at the same location. The SPICEX results shown in Fig. 16 of Farrokhrooz et al. (2017) were for relatively low winds (3–7 kn) and so should be comparable to the OBSANP results for the noise floor. The noise level at the bottom SPICEX hydrophone (4218 m) at 50 Hz (3×10^{-5} Pa^2/Hz or 75 dB re μPa^2/Hz) is in fact the same as the floor at the top OBSANP hydrophones at 40 Hz (Fig. 5), even though SPICEX occurred nearly a decade earlier. Farrokhrooz et al. (2017) extrapolated the SPICEX measurements to the seafloor for comparison with CHURCH ANCHOR and CHURCH OPAL. The median floor at the bottom hydrophone during OBSANP at 40 Hz of about 4×10^{-7} Pa^2/Hz (Fig. 5) is about 10 dB lower than the extrapolated noise level in Farrokhrooz et al. (2017), however, suggesting that the extrapolation did not accurately capture the decrease in the noise floor below the surface conjugate depth.

In 1973, Morris suspended a receiving array from R/P FLIP during the CHURCH ANCHOR exercise, where the bottom was at 5322 m and the conjugate depth was 4420 m.

The spectra for the three deepest sensors, on average 172 m off the bottom, show the typical mixture of a wind-associated flat spectrum at high frequencies, merging with a lower frequency floor shaped like f^{-2}. The apparent floor is more than 10 dB higher than that of OBSANP for $50 < f < 800$ Hz (Morris, 1978, Fig. 13). However, as Morris points out, the exercise was near major shipping lanes and although "attempts were made to remove the effects of local ships," the levels may be "slightly high compared to measurements made at other locations." Another possible explanation for the higher noise floor is that the CHURCH ANCHOR measurements contained some residual contamination because the array was suspended from R/P FLIP rather than moored to the seafloor, even though elaborate measures were taken to isolate the hydrophones from vibrations of the supporting cable.

The 1975 CHURCH OPAL exercise was conducted in the eastern subtropical Pacific at a location about 500 km south of OBSANP, with water depth 4850 m and conjugate depth 4060 m. The deepest sensor, 30 m off the bottom, gave an acoustic floor about 5 dB lower than reported here, but it was only resolved over the range $50 < f < 200$ Hz. The spectrum at higher frequencies is clearly determined by local wind, not distant shipping (Gaul et al., 2007, Fig. 19, and Shooter et al., 1990). Shooter et al. (1990) attributed the low noise level at the seafloor during CHURCH OPAL at least in part to bathymetric shielding by the Moonless Mountains to the north. Although there are several local small seamounts to the north, northwest, and west of the OBSANP site (Stephen et al., 2014), it seems unlikely that they would provide the same degree of bathymetric shielding as the Moonless Mountains, perhaps accounting in part for the slightly higher floor during OBSANP. It is also possible that the lower floor during CHURCH OPAL is due in part to less vigorous shipping in that era (e.g., McDonald et al., 2006; Andrew et al., 2002).

For $25 < f < 200$ Hz, the median acoustic floor at the deepest OBSANP sensor, node 148, is the same, within a few dB, as the pressure spectrum at ACO for the lowest overhead wind (Duennebier et al., 2012, Fig. 6). At higher frequencies, the OBSANP level is perceptibly smaller. The bottom at ACO, 100 km North of Oahu, is about 300 m shallower than at OBSANP and the average conjugate depth, 4542 m, nearly a kilometer deeper.

Finally, Reeder et al. (2011) reported spectra, for an average depth of 122 m, obtained in the Tongue of the Ocean. Although these measurements are in a vastly different geoacoustic setting than the measurements discussed above, they do provide information on the noise floor in the absence of shipping. For 100–200 Hz, spectra for the lowest OBSANP hydrophone (node 148) and TOTO are nearly the same, with OBSANP 3 dB above TOTO at 50 Hz and 6 dB below TOTO at 600 Hz. The similarity is remarkable given the different environments.

C. The high frequency acoustic beam

There are two striking features of the horizontal beam: (a) over a wide range of frequency, the width measured in vertical wave number is constant, and (b) the power in the

J. Acoust. Soc. Am. **143** (2), February 2018

Berger et al.   1231

beam itself falls with frequency faster than the omnidirectional power.

The 10 m spacing of the sub-array elements means the wave number spectrum is aliased for frequencies above 75 Hz, and the wave number resolution is coarse because of the small number of nodes. The Nyquist frequency in vertical wave number, $\kappa_{z,N} = \pi/10$ radians/m is reached at $f = C\kappa_{z,N}/(2\pi) \approx 75$ Hz for a sound speed of $C = 1530$ m/s. For 150 Hz, the power in the horizontal is contaminated by the alias from $2\kappa_{z,N}$, etc. Thus, the observed fall in the beam power is only an upper bound. Despite the contamination by high wave number aliases, the strength of the beam relative to the off-axis power clearly falls with frequency (Figs. 10 and 11).

From measurements during CHURCH ANCHOR, Anderson (1979, Fig. 11), found the acoustic energy horizontally polarized, with HPBS at 100 Hz of 15 and 10 degrees for depths of 3781 m and 4816 m, respectively. The low wind speed, averaging 2.6 m/s, and horizontal polarization together indicate the noise source was distant shipping. This is consistent with our measurement of 11° for the OBSANP acoustic floor at 100 Hz.

The acoustic floor measured in the sound channel is also horizontally polarized, but the HPBW for low frequencies has a constant angle rather than constant wave number. Baggeroer et al. (2005, Fig. 17), selected "quiescent spectra" from data of an array near the sound speed minimum where the ocean depth was 1800 m. For frequencies up to 50 Hz, their MVDR frequency-wave number spectrum (minimum variance, distortionless response, van Trees, 2004) show the energy to be horizontally polarized. As we find, the beam appears to vanish for frequencies below ≈ 6 Hz. More interestingly, the spectra shows a uniform phase speed equivalent to a beam width in this band of ±12.3°. Farrokhrooz et al. (2017, Fig. 9) obtained a similar result, with beam width ±17°. These results illustrate the quandary addressed by Dashen and Munk (1984): surface sources cannot yield geometric rays with turning points within the low velocity zone.

D. The high frequency geoacoustic model

Consider a deep-water, non-polar ocean with a sound speed channel and let there be numerous point radiators spottily distributed over the surface at distances outside the direct path range. In this case, the deep receivers are in the shadow zone (Farrell and Munk, 2013, Fig. 3), and energy arrives over paths with turning points below the conjugate depth that reflect from the sea surface [refracted then surface-reflected (RSR)].

1. Source physics

Because the sound speed exhibits relatively small variation with depth, long-range propagation to receivers beneath the conjugate depth is driven by the portion of the source's radiation pattern which is close to horizontal. For the OBSANP case, the ray with a turning point at 5000 m was emitted at the surface at an angle of 10.2 degrees. At 4000 m, the turning ray was launched at an angle of 4.9 degrees. Thus, only a 5-degree range of the source radiation

pattern is sampled. Above the bottom, the hydrophone is sensitive to all rays that turn at its position or deeper. Assuming sources are well distributed in range, the angular spread at 4000 m is ±9° for the OBSANP profile, and the spread should decrease as the measurement point deepens.

These angular values depend on the near surface sound speed. A 7° drop in temperature (for the subtropical Pacific, equivalent to a 6–9 degree increase in latitude) gives a 30 m/s decrease in sound speed. In this case, the launch angles for 4000 m and 5000 m turning points are 12 and 15 degrees, respectively. Thus, rays from more northerly sources have steeper launch angles.

2. Path physics

Rays with deep turning points can be blocked by topography and attenuated by bathymetry. The spectra obtained by Reeder et al. (2011) were from a site with extreme topographic blocking. Bathymetric attenuation is subtler. The effect begins at the source location: if the ocean is too shallow, rays with deep turning points will be immediately attenuated.

The bathymetry along 143.5° West, from 35° to 50° North, is profiled in Gaul et al. (2007, Fig. 8): the ocean from the Mendocino fracture zone (40° N) to the end of the profile is uniformly shallower than 5000 m. The situation will be similar at OBSANP, which is 6° E of the profile latitude: shallow rays from surface sources more northerly than the Mendocino fracture zone will have many interactions with the bottom and experience strong attenuation.

From the OBSANP perspective, there is deep ocean out to about 800 km for the 180° Northerly arc from East to West. Beyond, the zone of deep water narrows to a 45° arc, trending from NW to W. These are the zones most conducive to long range propagation from surface sources to deep receivers.

Anderson, V. C. (**1979**). "Variation of the vertical directionality of noise with depth in the North Pacific," J. Acoust. Soc. Am. **66**(5), 1446–1452.

Andrew, R. K., Howe, B. M., Mercer, J. A., and Dzieciuch, M. A. (**2002**). "Ocean ambient sound: Comparing the 1960's with the 1990's for a receiver off the California coast," Acoust. Res. Lett. Online **3**, 65–70.

Ardhuin, F., Lavanant, T., Obrebski, M., Marié, L., Royer, J.-Y., d'Eu, J.-F., Howe, B. M., Lukas, R., and Aucan, J. (**2013**). "A numerical model for ocean ultra low frequency noise: Wave-generated acoustic-gravity and Rayleigh modes," J. Acoust. Soc. Am. **134**, 3242–3259.

Ardhuin, F., Stutzmann, E., Schimmel, M., and Mangeney, A. (**2011**). "Ocean wave sources of seismic noise," J. Geophys. Res. **116**, C09004, https://doi.org/10.1029/2011JC006952.

Audoly, C., Rousset, C., and Leissing, T. (**2014**). "AQUO Project—Modelling of ships as noise source for use in an underwater noise footprint assessment," in *Proceedings of Inter.noise 2014, 43rd International*

Congress on Noise Control Engineering, November 16–19, Melbourne, Australia, pp. 1–10.

Baggeroer, A. B., Scheer, E. K., and The NPAL Group (**2005**). "Statistics and vertical directionality of low-frequency ambient noise at the North Pacific Acoustic Laboratory site," J. Acoust. Soc. Am. **117**(3), 1643–1665.

Buckingham, M. J., and Potter, J. R. (**1995**). *Sea Surface Sound'94* (World Scientific, Hackensack, NJ), 494 pp.

Dashen, R., and Munk, W. (**1984**). "Three models of global ocean noise," J. Acoust. Soc. Am. **76**(2), 540–554.

Duennebier, F. K., Lukas, R., Nosal, E., Aucan, J., and Weller, R. (**2012**). "Wind, waves, and acoustic background levels at Station ALOHA," J. Geophys. Res. **117**, C03017, https://doi.org/10.1029/2011JC007267.

Evans, R. B., and Carey, W. M. (**2010**). "Basin scale computation of vertical and horizontal directivity of underwater ambient noise, due to shipping and wind," in *Proceedings of the 9th International Conference on Theoretical and Computational Acoustics*, September 7–11, Dresden, Germany, pp. 373–384.

Farrell, W. E., Berger, J., Bidlot, J.-R., Dzieciuch, M., Munk, W., Stephen, R. A., and Worcester, P. F. (**2016**). "Windsea behind a cold front and deep ocean acoustics," J. Phys. Oceanogr. **46**(6), 1705–1716.

Farrell, W. E., and Munk, W. (**2010**). "Booms and busts in the deep," J. Phys. Oceanogr. **40**, 2159–2169.

Farrell, W. E., and Munk, W. (**2013**). "Surface gravity waves and their acoustic signatures, 1–30 Hz, on the mid-Pacific sea floor," J. Acoust. Soc. Am. **134**(4), 3134–3143.

Farrokhrooz, M., Wage, K. E., Dzieciuch, M. A., and Worcester, P. F. (**2017**). "Vertical line array measurements of ambient noise in the North Pacific," J. Acoust. Soc. Am. **141**, 1571–1581.

Gaul, R. D., Knobles, D. P., Shooter, J. A., and Wittenborn, A. F. (**2007**). "Ambient noise analysis of deep ocean measurements in the northeast Pacific," IEEE J. Ocean. Eng. **32**(2), 497–512.

Guralnik, Z., Zabalgogeazcoa, X., Bourdelais, J., and Farrell, W. E. (**2013**). "Wave-wave interactions and deep ocean acoustics," J. Acoust. Soc. Am. **134**(4), 3161–3173.

Hasselmann, K. (**1963**). "A statistical analysis of the generation of microseisms," Rev. Geophys. **1**, 177–210, https://doi.org/10.1029/RG001i002p00177.

Janssen, P. A. E. M. (**2008**). "Progress in ocean wave forecasting," J. Comput. Phys. **227**, 3572–3594.

Kedar, S., Longuet-Higgins, M., Webb, F., Graham, N., Clayton, R., and Jones, C. (**2008**). "The origin of deep ocean microseisms in the North Atlantic ocean," Proc. R. Soc. London A **464**, 777–793.

Kerman, B. R. (**1988**). *Sea Surface Sound, Natural Mechanisms of Surface Generated Noise in the Ocean* (Kluwer Academic Publishers, Amsterdam, the Netherlands), 639 pp.

Kerman, B. R., (**1993**). *Natural Physical Sources of Underwater Sound— Sea Surface Sound (2)* (Kluwer Academic Publishers, Amsterdam, the Netherlands), 750 pp.

Leckler, F., Ardhuin, F., Peureux, C., Benetazzon, A., Bergamasco, F., and Dulov, V. (**2015**). "Analysis and interpretation of frequency-wavenumber spectra of young wind waves," J. Phys. Oceanogr. **45**, 2484–2496.

Lenain, L., and Melville, K. (**2017**). "Measurements of the directional spectrum across the equilibrium saturation ranges of wind-generated surface waves," J. Phys. Oceanogr. **47**, 2123–2138.

Longuet-Higgins, M. S. (**1950**). "A theory of microseisms," Philos. Trans. R. Soc. London **243**, 1–35.

McDonald, M. A., Hildebrand, J. A., and Wiggins, S. M. (**2006**). "Increases in deep ocean ambient noise in the Northeast Pacific west of San Nicolas Island, California," J. Acoust. Soc. Am. **120**, 711–718.

Morris, G. B. (**1976**). "Church Anchor explosive source (SUS) propagation measurements from R/P Flip," SIO Reference 76-10.

Morris, G. B. (**1978**). "Depth dependence of ambient noise in the northeastern Pacific Ocean," J. Acoust. Soc. Am. **64**, 581–590.

Orcutt, J. A., Cox, C. S., Kibblewhite, A. C., and Kuperman, W. A. (**1993**). "Observations and causes of ocean and seafloor noise at ultra-low and very-low frequencies," in *Natural Physical Sources of Underwater Sound, Sea Surface Sound Vol. 2*, edited by B. R. Kerman (Kluwer Academic Publishers, Amsterdam, the Netherlands), pp. 203–232.

Peureux, C., and Ardhuin, F. (**2016**). "Ocean bottom pressure records from the Cascadia array and short surface gravity waves," J. Geophys. Res. **121**, 2862–2873, https://doi.org/10.1002/2015JC011580.

Reeder, D. B., Sheffield, E. S., and Match, S. M. (**2011**). "Wind-generated ambient noise in a topographically isolated basin: A pre-industrial area proxy," J. Acoust. Soc. Am. **129**, 64–73.

Shooter, J. A., DeMary, T. E., and Wittenborn, A. F. (**1990**). "Depth dependence of noise resulting from ship traffic and wind," IEEE J. Ocean. Eng. **15**(4), 292–298.

Sotirin, B. J., and Hodgkiss, W. S. (**1990**). "Fine-scale measurements of the vertical ambient noise field," J. Acoust. Soc. Am **87**(5), 2052–2063.

Stephen, R. A., Worcester, P. F., Udovydchenkov, I. A., Aaron, E., Bolmer, S. T., Carey, S., McPeak, S. P., Swift, S. A., and Dzieciuch, M. A. (**2014**). "Ocean bottom seismometer augmentation in the North Pacific (OBSANP)—Cruise Report," Technical Report No. WHOI-2014-03 (Woods Hole Oceanographic Inst., Woods Hole, MA).

van Trees, H. L. (**2004**). *Detection, Estimation and Modulation Theory* (Wiley, New York).

Wagstaff, R. A. (**2005**). "An ambient noise model for the Northeast Pacific Ocean Basin," IEEE J. Oceanic Eng. **30**, 286–294.

Wilson, J. H. (**1980**). "Low-frequency wind-generated noise produced by the impact of spray with the ocean's surface," J. Acoust. Soc. Am. **68**, 952–963.

Wilson, J. H. (**1983**). "Wind-generated noise modeling," J. Acoust. Soc. Am. **73**(1), 211–216.

Worcester, P. F., Carey, S., Dzieciuch, M. A., Green, L. L., Horwitt, D., Lemire, J. C., and Norenberg, M. (**2009**). "Distributed vertical line array (DVLA) acoustic receiver," in *Proceedings of the 3rd International Conference on Underwater Acoustic Measurements: Technologies and Results*, June 21–26, Nafplion, Greece, pp. 113–118.

Worcester, P. W., Dzieciuch, M. A., Mercer, J. A., Andrew, R. K., Dushaw, B. D., Baggeroer, A. B., Heaney, K. D., D'Spain, G. L., Colosi, J. A., Stephen, R. A., Kemp, J. N., Howe, B. M., Uffelen, L. J. V., and Wage, K. E. (**2013**). "The North Pacific Acoustic Laboratory deep-water acoustic propagation experiments in the Philippine Sea," J. Acoust. Soc. Am. **134**, 3359–3375.

Yurovskaya, M., Dulov, V. A., Chapron, B., and Kudryavtsev, V. N. (**2013**). "Directional short wind wave spectra derived from the sea surface photography," J. Geophys. Res. **118**, 4380–4394, https://doi.org/10.1002/jgrc.20296.